Applied Materials Today 8 (2017) 125–131

Contents lists available at ScienceDirect

Applied Materials Today

journal homepage: www.elsevier.com/locate/apmt

Hydrogen evolution and capacitance behavior of Au/Pd nanoparticle-decorated graphene heterostructures

Peter S. Toth[a,*,1], Matěj Velický[a,*,2], Thomas J.A. Slater[b], Stephen D. Worrall[a,3], Sarah J. Haigh[b]

[a] School of Chemistry, University of Manchester, Oxford Road, Manchester M13 9PL, UK
[b] School of Materials, University of Manchester, Oxford Road, Manchester M13 9PL, UK

ARTICLE INFO

Article history:
Received 19 December 2016
Received in revised form 21 July 2017
Accepted 24 July 2017

Keywords:
Graphene
Metal nanoparticles
Electron tomography
Hydrogen evolution
Capacitance

ABSTRACT

The outstanding properties of two-dimensional materials such as graphene offer the possibility to produce novel hybrid materials with boosted functionality for use in catalysis and electrochemical energy storage. The hydrogen evolution reaction and interfacial capacitance performance of monolayer graphene sheets decorated with various metal nanoparticles are studied herein. Chemical vapor deposition grown graphene monolayer was decorated with Au and/or Pd nanoparticles, either on one side or both sides, forming single- or bi metal graphene heterostructures. These asymmetrically decorated graphene nanocomposites were characterized using high-resolution scanning transmission electron microscopy and 3D electron tomography. Electrochemical characterization reveals enhanced hydrogen evolution activity and outstanding capacitance for the resultant composite materials in comparison to pristine graphene and other recently developed graphene-based energy storage devices.

1. Introduction

Concerns about atmospheric pollution and the sustainability of fossil fuel supplies have led to increased interest in the use of graphene (GR)-based materials for use in electrochemical energy storage and conversion technologies such as the hydrogen evolution reaction (HER). Several well constructed GR-based hybrid materials have been reported recently, showing extraordinary catalytic activity for the HER [1–3]. Pt with a catalytic activity (represented by Tafel slope) of ~30 mV dec^{-1} at low overpotential has long been established as the best HER catalyst [4]. However, materials such as transition metal dichalcogenides (TMDCs) [5–8], nanocrystalline transition metal carbides (M_3Cs) [9], and other metals (Pd, Au, Cu) [1,10–12] compare favorably in comparison to Pt when used either in their pristine form or as reduced graphene oxide (rGO)-based composites, with Tafel slopes of 56–65 mV dec^{-1}, 39–45 mV dec^{-1}, and 46–90 mV dec^{-1}, respectively.

There has been a recent upsurge of interest in the applications of graphene-based materials in electrochemical energy storage because of their beneficial physical properties such as mechanical strength, high-specific surface area, and high electrical and thermal conductivity [13–17]. Most porous graphene-based materials are formed from liquid-phase exfoliation (LPE) flakes, and although they have a high-specific surface area, they have poor electrical conductivity. In comparison, graphene prepared in a truly two-dimensional form, for example by chemical vapor deposition (CVD) growth, has a high-specific surface area and high electrical conductivity [18]. However, functionalization of CVD graphene has associated challenges. Organic/water interfaces enable the assembly of low-dimensional metallic, semi-conducting, and carbon materials (graphene and carbon nanotubes). The polarizable liquid/liquid interfaces, *i.e.* the interfaces between two immiscible electrolyte solutions (ITIES), could allow the reversible interfacial assembly of such nanostructures [19–21]. Recently, we reported on the assembly of monolayer graphene at the ITIES and its *in situ* functionalization utilizing both spontaneous and electrochemical deposition [22,23] of Au/Pd nanoparticles (NPs), deposited either

Abbreviations: CVD, chemical vapor deposition; GR, graphene; Pd/GR, palladium NPs on the topside of graphene; Au/GR, gold NPs on the topside of graphene; GR/Pd, palladium NPs on the underside of graphene; Au/GR/Pd, gold NPs on the topside and palladium NPs on the underside of graphene; 2D, two-dimensional; 3D, three-dimensional; HAADF-STEM, high-angle annular dark-field scanning transmission electron microscope; EDXS, energy-dispersive X-ray spectroscopy; PMMA, polymethyl methacrylate.

* Corresponding authors.
E-mail addresses: peter.toth@iit.it (P.S. Toth), matej.velicky@manchester.ac.uk (M. Velický).
[1] Present address: Graphene Labs, and iCub Facility, Istituto Italiano di Tecnologia, Via Morego 30, 16163 Genoa, Italy.
[2] Present address: Centre for Nanostructured Media, School of Mathematics and Physics, Queen's University Belfast, University Road, Belfast BT7 1NN, UK.
[3] Present address: School of Earth and Environmental Science, University of Manchester, Oxford Road, Manchester M13 9PL, UK.

http://dx.doi.org/10.1016/j.apmt.2017.07.008

on the top or on the bottom, or asymmetrically with two different elements on either side of the graphene sheet. This results in a "sandwich" type mono- or bi-metal graphene heterostructure. These composites were named mono- (Pd/GR, GR/Pd, Au/GR) or bi-metal (Au/GR/Pd) graphene nanocomposites. Furthermore, we also demonstrated the wide range of opportunities offered by the polarizable organic/water interface and used it as a platform for the assembly of liquid-phase exfoliated MoS_2 flakes. The exfoliated MoS_2 flakes, as well as synthetically grown vertically aligned MoS_2 nanosheets, were used to construct various CVD GR-based heterostructures [24].

Herein, we report on the electrocatalytic and capacitance performance of Au and Pd metal NP-decorated graphene heterostructures using a microscale electrochemical technique. Pd functionalization on either the topside or underside of the graphene monolayer affects the catalytic efficiency for the HER. Additionally the bi-metal GR composite exhibits enhanced capacitive performance.

2. Material and methods

2.1. Materials

Lithium perchlorate ($LiClO_4$, ≥99.5%), tetrabutylammonium perchlorate ($TBAClO_4$, ≥99.0%), ammonium tetrachloropalladate (II) ($(NH_4)_2PdCl_4$, 99.995%), and bis(pentamethylcyclopentadienyl) iron(II) ($Me_{10}FeCp_2$, decamethylferrocene (DecMFc), 97%) were purchased from Sigma–Aldrich, UK. Hydrogen tetrachloroaurate (III) trihydrate ($HAuCl_4$, 99.99%) was obtained from Alfa Aesar, UK. All metals were purchased from Advent Research Materials, UK. The organic phase was formed from mixtures of 1,2-dichloroethane (DCE, ≥99.8%) and di-n-butyl ketone (5-nonanone, 98%) purchased from Sigma–Aldrich and used as received. The aqueous solutions were prepared using deionized, ultra-pure water (18.2 MΩ cm, Milli-Q Direct 8, Merck Millipore, USA). The Cu foil was etched from underneath the pristine or decorated graphene layers by 0.5 M ammonium persulfate (98%, Lancaster Synthesis Ltd., UK) aqueous solution. The CVD graphene was a gift from BGT Materials Ltd. (Manchester, UK) and was prepared using methods previously reported [25]. The high quality of the CVD grown monolayer graphene was confirmed by Raman spectroscopy (Supplementary Figure 1) [26,27].

2.2. Methods

High-angle annular dark-field (HAADF) scanning transmission electron microscope (STEM) imaging was performed on an FEI probe-corrected Titan G2 80–200 S/TEM with a high brightness X-FEG electron source and Super-X energy dispersive X-ray (EDX) silicon drift detectors (SDDs). The microscope was operated at an accelerating voltage of 80 kV with a beam current of 260 pA, a convergence angle of 21 mrad and a HAADF acceptance inner angle of 50 mrad. EDX spectrum images were acquired in the Bruker Esprit software using the Titan's Super-X detector system, with a total per pixel dwell time of 6 ms and an image size of 512 × 512 pixels. All EDX elemental maps have been filtered using a 3-pixel smoothing window in Esprit. A tilt series for HAADF-STEM tomography was acquired using Xplore3D acquisition software at angular increments of 1° from −50° to +65°. Spatial image alignment was performed using cross-correlation of HAADF images in FEI's Inspect3D software package. Tilt axis alignment was also undertaken in Inspect3D followed by the use of a simultaneous reconstruction technique (SIRT) algorithm to perform the reconstruction with 20 iterations. Segmentation of Au and Pd voxels was performed manually in Avizo; the segmentation was guided *via* comparison to the EDX spectrum images acquired of the same sample area. Visualization of the 3D reconstructions was also performed in the Avizo software package.

Raman spectroscopy was measured with an inVia Renishaw spectrometer (Renishaw PLC, UK), using a 532 nm laser excitation wavelength and a ×100 objective, resulting in a laser spot size of *ca.* 0.8 μm^2. The atomic force microscopic (AFM) characterization was carried out using a Bruker MultiMode 8 equipment (operated in "Peak Force" tapping mode) on samples transferred to a Si/SiO_2 wafer. The CVD graphene layers on a Cu foil were spin-coated with 3% 950 K polymethyl methacrylate (PMMA) solution in anisole (MicroChem Corp.) at 3000 rpm for 60 s using a SPIN200i-NPP spin processor (SPS-Europe B.V., The Netherlands) in preparation for transfer.

Aqueous droplets of either 6 M LiCl or 0.1 M HCl in 6 M LiCl used for the electrochemical measurements were formed using a borosilicate micropipette (*ca.* 1 μm internal tip diameter) and a pneumatic microinjector (PV820 Pneumatic PicoPump, WPI, USA). The motion of the micropipette was controlled electronically using MX7630 micromanipulator and MC1000e motion controller (Siskiyou, OR, USA). An Ag/AgCl reference electrode (RE) and Pt counter electrode (CE) were embedded in the micropipette [28,29]. In this three-electrode configuration, the localized HER and capacitance of the interfacial area between the droplet and sample surface were measured using a PGSTAT302N potentiostat (Metrohm Autolab B.V., The Netherlands). Electrochemical measurements were performed at ambient temperature (22–24 °C). The potential, which is measured against Ag/AgCl reference electrode in 6 M LiCl ($E_{Ag/AgCl}$ (6 M LiCl)), is shifted by *ca.* +0.19 V with respect to the standard hydrogen electrode (SHE) scale. All the potentials (E_{RHE}) reported in this work are plotted on the reversible hydrogen electrode (RHE) scale, calculated from Eq. (1).

$$E_{RHE} = E_{measured} - 0.059 \times pH + E_{Ag/AgCl}(6\,M\ \ LiCl) \quad (1)$$

where E_{RHE} is the potential of the RHE, $E_{measured}$ is the measured potential, and $E_{Ag/AgCl}$ (6 M LiCl) is the potential of the Ag/AgCl reference electrode in 6 M LiCl, shifted by *ca.* +0.19 V with respect to the standard hydrogen electrode scale. A schematic of the micro-droplet electrochemical setup and an optical micrograph of a contacted droplet on a Pd/GR sample can be seen in Scheme 1A and B, respectively.

3. Results and discussion

3.1. Preparation and transfer of the pristine and decorated GR layers

NP-decorated CVD GR layers were prepared by metal NP deposition on the monolayer GR assembled at the ITIES, as reported previously [22,23]. Briefly, three kinds of functionalization of graphene were carried out: topside (Scheme 2Aa), underside (Scheme 2Ab), and dual/asymmetric (Scheme 2Ac) decoration.

The topside decoration of graphene (GR) was performed using a simple galvanic displacement for the nucleation of Au or Pd NPs (hereafter, Au/GR or Pd/GR) [30]. The underlying copper foil below graphene acts as an electron donor and transfers electrons to the tetrachloro-metal complex on the other side (top) [23]. Another simple, spontaneous Pd NP deposition technique was applied at the interface-assembled CVD GR to decorate the underside of graphene. An interfacial redox reaction between bis(pentamethylcyclopentadienyl) iron(II) (DecMFc), which is the organic-phase electron donor, and $PdCl_4^{2-}$ contained in the aqueous phase creates GR/Pd layers [22]. The combination of these two methods (the topside and underside decoration) was applied to obtain an asymmetric functionalization of the graphene layer at the ITIES, producing bi-facially decorated monolayer graphene

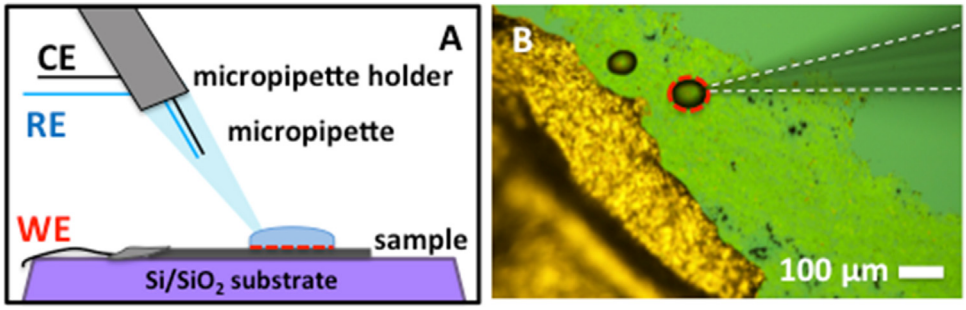

Scheme 1. Electrochemical investigation setup. (A) Schematic of the micro-droplet electrochemical approach, depicting the Si/SiO_2 wafer with sample, the red dash line shows the working area (working electrode, WE) contacted *via* silver epoxy and copper wire; a micropipette, which contains RE and CE, and is connected to a micromanipulator and microinjector *via* the micropipette holder. (B) Optical micrograph of a droplet deposited on the surface of Pd/GR specimen; the investigated droplet is marked with a red dashed line. The silver paint and the uncovered Si/SiO_2 wafer are in the left and right corners of micrograph, respectively. The dashed white lines indicate the shadow of the micropipette connected to the droplet. (For interpretation of the references to color in this scheme legend, the reader is referred to the web version of this article.)

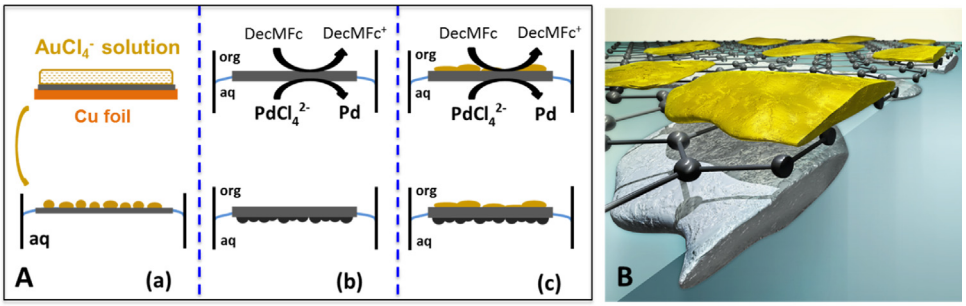

Scheme 2. Decoration process of CVD graphene. (A) Schemes of topside (a), underside (b), and asymmetric two-sided (c) decoration processes of graphene with Au and Pd NPs. Graphene gray solid rectangle; Au is yellow and Pd is black. (B) Schematic figure of the bi-facially decorated GR single-layer: Au/GR/Pd bi-metal sandwich, with the Au (yellowish) and Pd ('metallic silver' colored) NPs on the topside and underside, respectively. (For interpretation of the references to color in this scheme legend, the reader is referred to the web version of this article.)

with Au NPs on the topside and Pd NPs on the underside of graphene, respectively (hereafter, Au/GR/Pd). Scheme 2B depicts a three-dimensional (3D) illustration of Au/GR/Pd "sandwich" heterostructure.

In the case of topside decoration of graphene (also the first step of the Au/GR/Pd preparation), 1 mM $HAuCl_4$ or $(NH_4)_2PdCl_4$ aqueous solution was placed on top of a CVD GR layer lying on Cu foil (GR/copper); then, after 1 min, the Au or Pd NPs were spontaneously deposited, respectively. The as-formed Au/GR/copper or Pd/GR/copper stacks were subsequently placed in 0.5 M ammonium persulfate solution to remove the underlying copper foil by etching. The resulting Au/GR or Pd/GR layers were cleaned three times by transfer to deionized water. These topside functionalized graphene monolayers were then transferred either onto an Si/SiO_2 substrate for electrochemical measurements or, in the case of Au/GR, onto the surface of an aqueous solution containing 1 mM $(NH_4)_2PdCl_4$ salt to perform the second step of Au/GR/Pd preparation. Briefly, 2 mM DecMFc (in the DCE/5-nonanone mixture) was layered carefully on top of the free-standing Au/GR film floating on the aqueous solution layer in order to induce the deposition of Pd nanoparticles on the underside of the graphene monolayer yielding an Au/GR/Pd sandwich. This asymmetrically functionalized graphene/metal NP heterostructure was then transferred onto Si/SiO_2 wafers for electrochemical measurements. Some of the graphene monolayers were also transferred from the Cu foil onto the surface of aqueous solutions containing the $PdCl_4^{2-}$ complex for the underside decoration to give GR/Pd. The transfer from Cu foil was carried out by spin-coating the CVD GR with *ca.* 100 μm PMMA thick film on the Cu foil [22], resulting in a PMMA/GR/Cu stack. The Cu foil was etched from underneath the PMMA/GR stack using a 0.5 M ammonium persulfate solution, and the remaining PMMA/GR stack was "fished out" with a Si/SiO_2 wafer, and then cleaned three times by deionized water. This PMMA/GR stack on a Si/SiO_2 wafer was then transferred onto the surface of an aqueous phase, containing the 1 mM $(NH_4)_2PdCl_4$ salt, and carefully covered by a DecMFc-free organic phase (DCE/5-nonanone mixture, 1:4 by volume ratio). After a while, the PMMA/GR stack became invisible as the PMMA was dissolved from the top of GR by the organic solvent mixture. The organic phase was then replaced with a fresh batch containing 2 mM DecMFc, to perform the underside functionalization. These underside functionalized CVD GR layers were then transferred onto Si/SiO_2 wafers for electrochemical measurements. In all cases of the underside decoration, 0.1 M $TBAClO_4$ and 0.1 M $LiClO_4$ supporting electrolytes were used in the organic (org) and aqueous (aq) phases, respectively.

3.2. *Transmission electron microscopy characterization of decorated graphene layers*

The HAADF-STEM image (Fig. 1A) shows the Au/GR/Pd sandwich heterostructure. The contrast of this imaging technique scales with atomic number, so the heavier Au NPs are visualized as regions of high brightness while the lighter Pd NPs are visualized as regions of medium brightness (gray tones). Graphene monolayer can also be seen between the topside and underside-deposited particles as a faint, very low brightness membrane.

In the cases of both topside and underside decorations, the STEM-HAADF images at higher magnification reveal that the nanostructures consist of smaller NPs [23]. The size distribution of the Au and Pd NPs on the top of graphene was *ca.* 10–90 nm (Au/GR) and 20–80 nm (Pd/GR), respectively. Similarly, in the case of Pd decoration of the underside of CVD GR (GR/Pd), some small round-shaped individual Pd particles were found with sizes of 10–80 nm (Supplementary Figure 2). Elemental analysis was carried out using

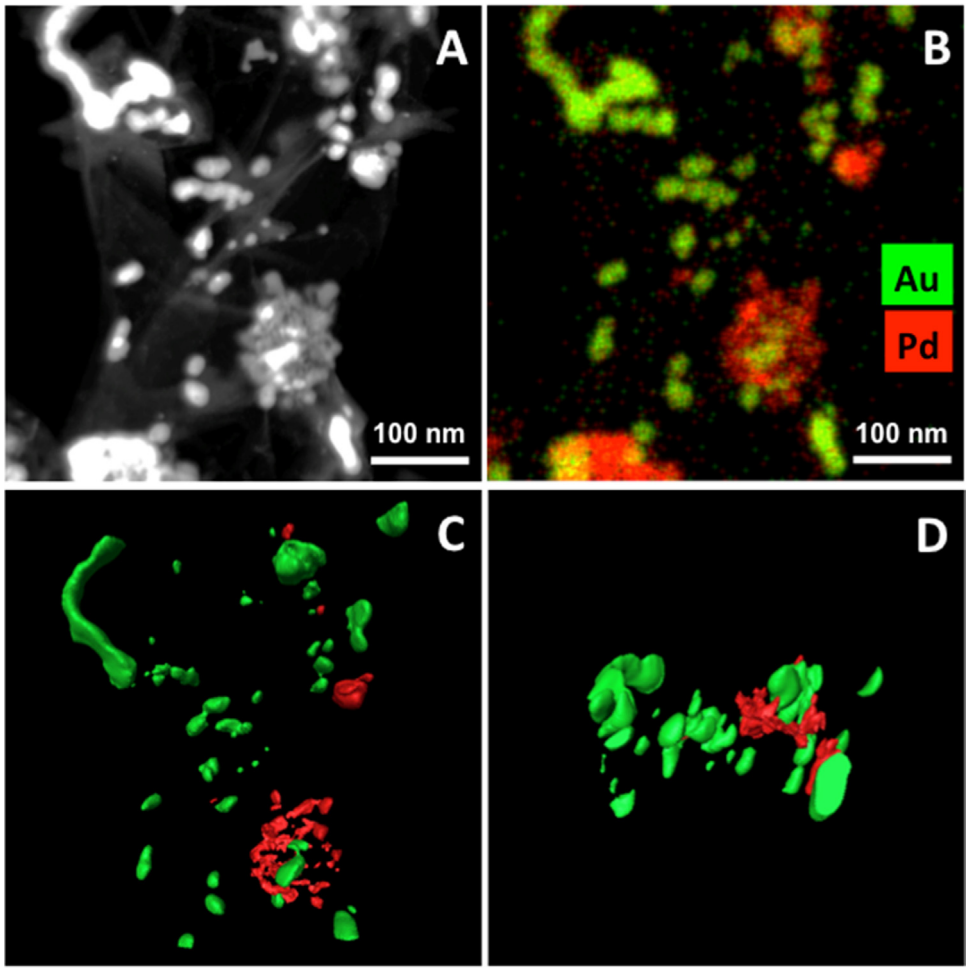

Fig. 1. STEM characterization of Au/GR/Pd sandwich. (A) STEM-HAADF image of the graphene-based gold (on top) and palladium (bottom) decorated nanocluster. Different shades of gray corresponding to Au and Pd and the graphene support (light gray). (B) A STEM-EDXS elemental map acquired in the same region as A; this composite image shows the presence of Au (green) and Pd (red). 3D surface visualization of the segmented Au/GR/Pd sandwich analyzed by HAADF-STEM tomography shown from the top (C) and from the side (D) views; the segmentation was guided by the STEM-EDXS elemental maps. (For interpretation of the references to color in this figure legend, the reader is referred to the web version of this article.)

EDX spectroscopy (EDXS), which was subsequently used to guide the segmentation of a 3D reconstruction from a HAADF-STEM tilt series [31,32]. The STEM-EDXS chemical map (Fig. 1B) and a segmented 3D visualization of a HAADF-STEM tomography reconstruction are shown from the top- (Fig. 1C) and side-views (Fig. 1D), where the green and red colors correspond to the Au and Pd NPs, respectively. Some parts of the sample are decorated only on the topside by Au or the underside by Pd NPs, respectively, but two parts show clearly the "sandwich" heterostructure. The red circular structure with the green spot in the middle (Fig. 1B) corresponds to Pd aggregates underneath the GR layer with an Au nanostructure on the top, which is confirmed by the side-view 3D STEM-EDXS image (Fig. 1D). More evidence for the dual-decorated CVD GR can be found in previous reports [22,23]. For example, the graphene-based metal nanoclusters were previously characterized using atomic force and electron microscopy techniques (SEM and STEM), and the location of the metal nanostructures underneath the graphene layer has been identified from the position shift of graphene Raman modes (G, 2D) toward higher frequencies and the intensity changes of the Raman modes (I_D/I_G, I_{2D}/I_G) [22]. The dual-decorated "bi-metal-graphene sandwiches" were previously studied using Raman spectroscopy, X-ray photoelectron spectroscopy, STEM, and electron energy loss spectroscopy (EELS) [23]. Additionally, the aligned HAADF-STEM tilt series and a rotating view of the segmented reconstruction for the asymmetrically dual-decorated Au/GR/Pd heterostructures can be found in Supplementary Information (Movie S1, S2). In the case of Movie S1, the heavier (and therefore brighter) Au NPs can be seen on the top, while the moderately heavy Pd NPs are at the bottom of the very light graphene support, which appears as a "shadow" during the rotation in the HAADF-STEM imaging (different tilt series of STEM-HAADF, and STEM-EDXS maps are also shown in Supplementary Figure 3). The 3D surface visualization of the segmented Au/GR/Pd analyzed by HAADF-STEM electron tomography (Movie S2) shows the surface visualization of the segmented Au NPs (green) on the topside and Pd NPs (red) on the underside of graphene layer.

3.3. *Electrochemical investigation of decorated graphene heterostuctures*

Electrochemical measurements using micro-droplets [28,29] were performed to explore the chemical and physical properties of these metal NP/GR heterostructures. Specifically, we have investigated the HER catalytic performance and the interfacial capacitance. The micro-droplets were 30–50 μm in diameter, and 3 individual droplets for each specimen were used for the analysis of each measurement. In order to assess the catalytic activity toward the HER, polarization curves of all the samples (GR, Pd/GR, GR/Pd, Au/GR, and Au/GR/Pd) were measured using aqueous droplets containing 0.1 M HCl and 6 M LiCl (Fig. 2A). It is

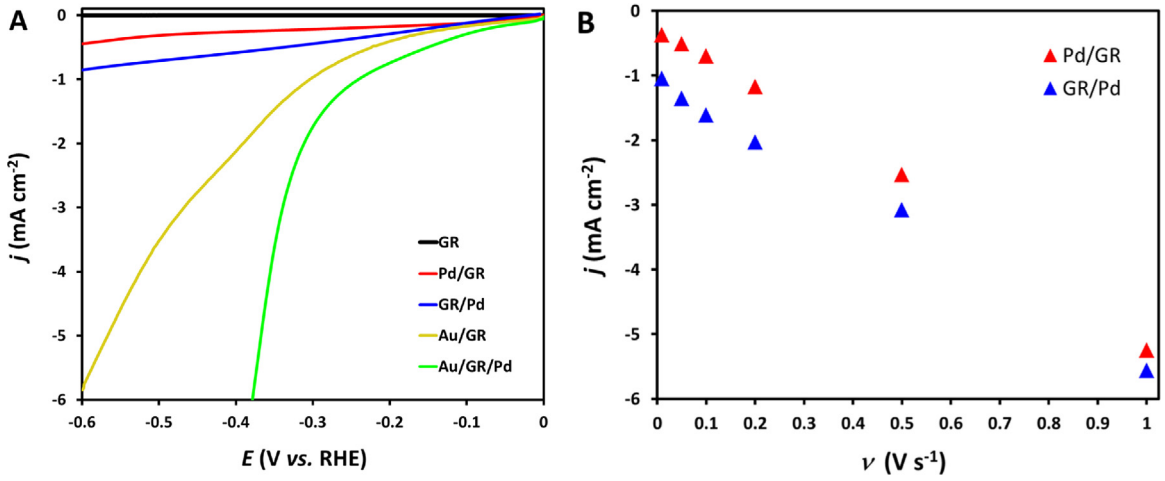

Fig. 2. Electro-catalytic activity of CVD GR-based nanoclusters. (A) The HER polarization curves obtained on the composite materials in 0.1 M HCl and 6 M LiCl, at 50 mV s^{-1} scan rate. (B) Plot of the current density for Pd/GR and GR/Pd specimens at −0.35 V as a function of different scan rates (ν).

well established that pristine GR is a poor HER catalyst, and only a small current density was also observed for Pd/GR or GR/Pd. However, the Au-decorated GR composites seem to be a more promising system. The Tafel slopes were estimated from the linear portions of the polarization curves (Fig. 2A) using Eq. (2):

$$\eta = a + b \times \log|j| \quad (2)$$

where η is the overpotential, j is the current density, b is the Tafel slope and a is the intercept ($\log j_0$, where j_0 is the exchange current density). The Tafel slopes of 171.8 ± 0.91, 153.7 ± 0.19, 124.4 ± 0.44, 110.4 ± 0.76, and 104.7 ± 0.72 mV dec^{-1} were found for GR, Pd/GR, GR/Pd, Au/GR, and Au/GR/Pd, respectively. All values were measured repeatedly in the three deposited micron-sized droplets for the different ranges of each sample. These values are comparable with the previously reported values for similar systems [1,10,33]. The Au/GR/Pd composite therefore displays the best activity with the smallest Tafel slope value of 104.7 ± 0.72 mV dec^{-1}. However, a lower Tafel slope was published recently, *i.e.* 46 mV dec^{-1} in 0.5 M H_2SO_4 solution for a Pd NP-decorated rGO-modified glassy carbon electrode [33]. In this case, the small rGO flakes could cause the higher activity due to increased density of rGO edges, similar to the case of ball-milled graphite, with more exposed edges showing a much better increased electro-catalytic performance for the oxygen reduction reaction (ORR) [34]. Decoration of rGO using either Pd, or Au, or both NPs has also been reported by Darabdhara et al. [12]. In the case of both Pd and Au NPs, 29.0 mV dec^{-1} Tafel slope was found, and additionally, an excellent electrocatalytic activity was observed even after 5000 sweep cycles.

Furthermore, the Tafel analysis allows us to extract the transfer coefficient (α), which is used for the kinetic evaluation of the HER process [35,36]. Fitting of the experimental data (using overpotential values calculated from linear parts of the Tafel plots) demonstrated a difference between the transfer coefficients of the various metal NP-graphene heterostructures. In the case of the pristine monolayer graphene, α is 0.34, while for the heterostructures, α was equal to 0.38, 0.47, 0.53, and 0.56 for Pd/GR, GR/Pd, Au/GR, and Au/GR/Pd, respectively. An inverse correlation is exhibited between the value of the Tafel slope and α, which is to be expected according to the Butler–Volmer equation [36]. The difference in the observed current densities, Tafel slopes, and α between the Pd/GR and GR/Pd as a function of scan rate (Fig. 2B) shows that there is a higher HER activity when the Pd NPs are lying under the monolayer GR as opposed to on top. Although there is the possibility of the Pd NPs under GR being exposed due to defects in GR, significant proton transfer is likely to have occurred in order to produce the observed enhanced HER activity [37]. Relating to the three reaction mechanisms in acidic media for the HER [38], the first is an initial discharge step ($b \approx 120$ mV dec^{-1}), followed by either an electrochemical desorption step ($b \approx 40$ mV dec^{-1}) or a recombination step ($b \approx 30$ mV dec^{-1}). Our Tafel slopes are in the range of 154 and 105 mV dec^{-1} for the studied heterostructures, which suggest that the process is a combination of the initial discharge and electrochemical desorption steps. To conclude this part, while quite diverse HER activities are observed for the various graphene-based metal nanocomposites, the additional Au-modified GR hybrids show more promising catalytic performance for HER compared to the Pd-only modified composites.

The capacitive performance of the metal NP/GR heterostructures was electrochemically tested by the determination of the electric double-layer capacitance (C) for each sample using the cyclic voltammetric measurements in a 6 M LiCl aqueous solution following Eq. (3):

$$C = \frac{1}{2\nu(E_{max} - E_{min})} \oint I(E)dE \quad (3)$$

where ν is the scan rate, I is the measured current, E is the applied potential and E_{max} and E_{min} are the maximum and minimum potentials applied during the voltammetric scan, respectively. The values of C are directly proportional to electrochemically active surface areas of the samples and were determined from cyclic voltammetry (CV) measurements in the potential window −0.4 V to 0.4 V in 6 M LiCl aqueous solution at various scan rates. The specific capacitance (C_{sp}, in mF cm^{-2}) values were calculated from C and geometric surface area values. The dependence of the C_{sp} on scan rate is depicted in Fig. 3A, showing the previously observed [15,39] inverse correlation with the increasing scan rate, arising from the diffusion-limited supply of ions. At 100 mV s^{-1}, the calculated specific capacitance for Au/GR/Pd (3.84 mF cm^{-2}) is approximately 3, 6, 70, and 870 times larger than that for Au/GR (1.15 mF cm^{-2}), GR/Pd (0.70 mF cm^{-2}), Pd/GR (56 μF cm^{-2}), and GR (4.4 μF cm^{-2}), respectively (Fig. 3A).

The C_{sp} decreases for example by 32.8% when the scan rate increases from 100 mV s^{-1} up to 3 V s^{-1} in the case of the pristine graphene, and similar downward trend is also observed for the other heterostructures. Considering novel hybrid materials for application in an electrochemical energy storage device, one of the most important behaviors for effective use is the cycling stability. Ideal supercapacitors should possess extremely high stability with minimal degradation in performance with repeated charge/discharge cycles, while pseudocapacitors typically sacrifice cycling stability for increased energy density [15]. Fig. 3B shows

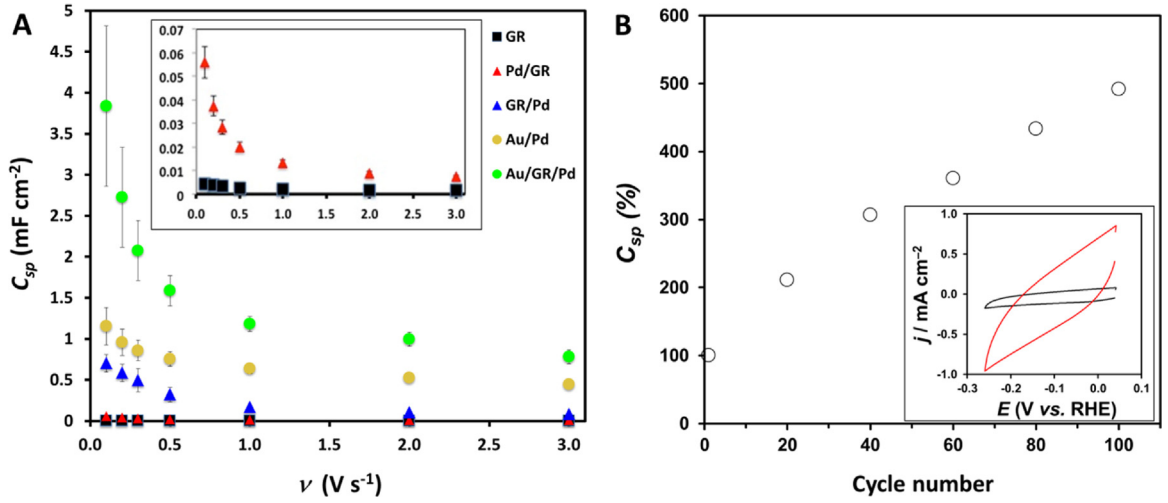

Fig. 3. Capacitive performance of the GR hybrid films. (A) Plot of the specific capacitance *versus* scan rate (ν). The inset in (A) shows the magnified response of GR and Pd/GR signals. (B) Plot of change in specific capacitance (%) with continued CV cycles of Au/GR/Pd nanocomposite; the 100th and 1st CVs after 100 cycles in 6 M LiCl aqueous solution are shown in the inset at 100 mV s^{-1} scan rate. The displayed errors are either standard deviations (arithmetic averages of multiple measured values) or absolute errors determined from best-fit errors.

the cycling stability of the Au/GR/Pd heterostructure over 100 CV cycles. There is a large increase (~400%) when comparing the C_{sp} values of the 100th and 1st cycles. This increased capacitance with continuous cycling merits careful consideration. It has been reported previously for reduced graphene oxide films, MoS_2 films and particularly for transition metal oxide films and was attributed to the partial exfoliation with continued ion intercalation/deintercalation increasing the active surface area, which was termed "electroactivation" [17,39,40]. Increased capacitance with continuous cycling has also been found for porous-type rGO electrodes, where rGO was decorated with flower-like MnO_2 nanostructures fabricated by electrodeposition [41]. These materials showed a dramatically increased specific capacitance using galvanostatic charge and discharge for about 1300 cycles. In this material, the rGO sheets can move to adjust to the different electrolyte ions, and the long time charging and discharging may also help the ions access all the graphene sheets to utilize the larger surface area. In contrast, our work relates to a CVD grown "two-dimensional" graphene layer with electro-deposited metal nanoparticles, and for this type of material, increased capacitance with continuous cycling has not been reported previously. One report for a CVD grown graphene foam ("three-dimensional") decorated by NiO nanoparticles, forming a NiO/3D graphene nanocluster, found that the specific capacitance increased by about 15% during the first 200 cycles, which was attributed to the "activation" process that allows the trapped ions to gradually diffuse out [42]. Therefore, in the case of our Au/GR/Pd heterostructure, the enhanced capacitive behavior could be explained by penetration of the electrolyte ions (Li^+, Cl^-) between the metal NPs and graphene layer modifying the surface, and a subsequent increase in the accessible electroactive area upon repeated cycling. This hypothesis is further supported by our observation that the highest C_{sp} was observed for the slowest cycling rate. Further investigations such as the exploration of different metal NPs, modified particle size and density and long-term stability studies will be required to optimize these heterostructures for specific applications.

4. Conclusions

In summary, either one or both sides of graphene monolayers were decorated with metal NPs to construct single-metal or bi-metal graphene heterostructures. A micro-droplet setup was employed to investigate the electrochemical performance of the GR-based hybrid materials as HER catalysts and electric double layer capacitors.

The different composites showed diverse catalytic activities, with the best Tafel slope for the HER found to be 104.7 mV dec^{-1} for the bi-metal Au/GR/Pd sandwich structure. This synthesis approach represents a unique and controllable platform to prepare asymmetrically functionalized 2D materials, which can provide important insights to optimize materials for applications in energy conversion and storage.

Functionalized CVD GR-metal nanocomposites show high capacitance values, *i.e.* 870 times larger in the case of Au/GR/Pd heterostructure, than that measured for pristine graphene and are also comparable with the capacitive activities of some recently reported energy storage device based on liquid-phase exfoliated MoS_2/GR heterostuctures [24,39,43]. Although all these measured capacitances are likely to be overestimated due to the increased surface area (real *versus* geometric) [24,43], herein we make a relative comparison between different heterostuctures with CVD graphene as the baseline. Additionally, cycling stability measurements demonstrated around a 400% increase in the specific capacitance, representing promising application for supercapacitor electrodes. The increase is suggested to be due to the electroactive area change, which most probably relates to increased surface area generated by electrolyte ions during the charge/discharge cycles [24,39–42].

Improved understanding of the electro-catalytic nature of bifacially functionalized graphene nanostructures is an essential step toward their exploitation in biphasic catalysis, such as HER or ORR at the ITIES [20,44,45]. Moreover, the interface-assembled fabrication of graphene composites is a promising platform for the synthesis of heterostructures *via* topside decoration using 2D materials exfoliated in the organic phase. This could potentially provide an alternative to the conventionally employed procedures, *i.e.* the use of a solid substrate [1,40,46].

Supplementary material

The Supplemental Information shows further spectroscopic and microscopic characterizations; the supplemental movies showing the HAADF-STEM and 3D electron tomography tilt series (Movie S1, S2) are provided.

Conflict of interest

The authors declare no competing financial interests.

Acknowledgement

The authors thank the U.K. EPSRC (grants EP/K007033/1, EP/K016954/1, EP/K016946/1, EP/M010619/1 and EP/G035954/1) for financial support. S.J.H. thanks the Defence Threat Reduction Agency Grant HDTRA1-12-1-0013.

Appendix A. Supplementary data

Supplementary data associated with this article can be found, in the online version, at doi:10.1016/j.apmt.2017.07.008.

References

[1] F. Li, L. Zhang, J. Li, X.Q. Lin, X.Z. Li, Y.Y. Fang, J.W. Huang, W.Z. Li, M. Tian, J. Jin, R. Li, Synthesis of Cu-MoS_2/rGO hybrid as non-noble metal electrocatalysts for the hydrogen evolution reaction, J. Power Sources 292 (2015) 15–22.
[2] P.V. Kamat, Graphene-based nanoarchitectures. Anchoring semiconductor and metal nanoparticles on a two-dimensional carbon support, J. Phys. Chem. Lett. 1 (2010) 520–527.
[3] Q. Xiang, J. Yu, Graphene-based photocatalysts for hydrogen generation, J. Phys. Chem. Lett. 4 (2013) 753–759.
[4] N.M. Marković, B.N. Grgur, P.N. Ross, Temperature-dependent hydrogen electrochemistry on platinum low-index single-crystal surfaces in acid solutions, J. Phys. Chem. B 101 (1997) 5405–5413.
[5] X. Zheng, J. Xu, K. Yan, H. Wang, Z. Wang, S. Yang, Space-confined growth of MoS_2 nanosheets within graphite: the layered hybrid of MoS_2 and graphene as an active catalyst for hydrogen evolution reaction, Chem. Mater. 26 (2014) 2344–2353.
[6] X. Yu, M.S. Prevot, N. Guijarro, K. Sivula, Self-assembled 2D WSe_2 thin films for photoelectrochemical hydrogen production, Nat. Commun. 6 (2015).
[7] Y. Li, H. Wang, L. Xie, Y. Liang, G. Hong, H. Dai, MoS_2 nanoparticles grown on graphene: an advanced catalyst for the hydrogen evolution reaction, J. Am. Chem. Soc. 133 (2011) 7296–7299.
[8] X. Chia, A. Adriano, P. Lazar, Z. Sofer, J. Luxa, M. Pumera, Layered platinum dichalcogenides (PtS_2, $PtSe_2$, and $PtTe_2$) electrocatalysis: monotonic dependence on the chalcogen size, Adv. Funct. Mater. 26 (2016) 4306–4318.
[9] X. Fan, Z. Peng, R. Ye, H. Zhou, X. Guo, M_3C (M: Fe, Co, Ni) nanocrystals encased in graphene nanoribbons: an active and stable bifunctional electrocatalyst for oxygen reduction and hydrogen evolution reactions, ACS Nano 9 (2015) 7407–7418.
[10] S. Sarkar, S. Sampath, Equiatomic ternary chalcogenide: PdPS and its reduced graphene oxide composite for efficient electrocatalytic hydrogen evolution, Chem. Commun. 50 (2014) 7359–7362.
[11] J. Li, P. Zhou, F. Li, J. Ma, Y. Liu, X. Zhang, H. Huo, J. Jin, J. Ma, Shape-controlled synthesis of Pd polyhedron supported on polyethyleneimine-reduced graphene oxide for enhancing the efficiency of hydrogen evolution reaction, J. Power Sources 302 (2016) 343–351.
[12] G. Darabdhara, M.A. Amin, G.A.M. Mersal, E.M. Ahmed, M.R. Das, M.B. Zakaria, V. Malgras, S.M. Alshehri, Y. Yamauchi, S. Szunerits, R. Boukherroub, Reduced graphene oxide nanosheets decorated with Au, Pd and Au-Pd bimetallic nanoparticles as highly efficient catalysts for electrochemical hydrogen generation, J. Mater. Chem. A 3 (2015) 20254–20266.
[13] L.L. Zhang, X. Zhao, H. Ji, M.D. Stoller, L. Lai, S. Murali, S. McDonnell, B. Cleveger, R.M. Wallace, R.S. Ruoff, Nitrogen doping of graphene and its effect on quantum capacitance, and a new insight on the enhanced capacitance of N-doped carbon, Energy Environ. Sci. 5 (2012) 9618–9625.
[14] Y. Lu, F. Zhang, T. Zhang, K. Leng, L. Zhang, X. Yang, Y. Ma, Y. Huang, M. Zhang, Y. Chen, Synthesis and supercapacitor performance studies of N-doped graphene materials using o-phenylenediamine as the double-N precursor, Carbon 63 (2013) 508–516.
[15] J. Chen, C. Li, G. Shi, Graphene materials for electrochemical capacitors, J. Phys. Chem. Lett. 4 (2013) 1244–1253.
[16] L. Zhang, F. Zhang, X. Yang, G. Long, Y. Wu, T. Zhang, K. Leng, Y. Huang, Y. Ma, A. Yu, Y. Chen, Porous 3D graphene-based bulk materials with exceptional high surface area and excellent conductivity for supercapacitors, Sci. Rep. 3 (2013) 1408.
[17] M. Beidaghi, C. Wang, Micro-supercapacitors based on interdigital electrodes of reduced graphene oxide and carbon nanotube composites with ultrahigh power handling performance, Adv. Funct. Mater. 22 (2012) 4501–4510.
[18] F. Xu, T. Lin, H. Bi, F. Huang, Graphene-like carbon with three-dimensional periodicity prepared from organic–inorganic templates for energy storage application, Carbon 111 (2017) 128–132.
[19] Y. Gründer, Q.M. Ramasse, R.A.W. Dryfe, A facile electrochemical route to the preparation of uniform and monoatomic copper shells for gold nanoparticles, Phys. Chem. Chem. Phys. 17 (2015) 5565–5568.
[20] X. Bian, M.D. Scanlon, S. Wang, L. Liao, Y. Tang, B. Liu, H.H. Girault, Floating conductive catalytic nano-rafts at soft interfaces for hydrogen evolution, Chem. Sci. 4 (2013) 3432–3441.
[21] H. Jensen, D.J. Fermin, J.E. Moser, H.H. Girault, Organization and reactivity of nanoparticles at molecular interfaces. Part 1. Photoelectrochemical responses involving TiO_2 nanoparticles assembled at polarizable water vertical bar 1,2-dichloroethane junctions, J. Phys. Chem. B 106 (2002) 10908–10914.
[22] P.S. Toth, Q.M. Ramasse, M. Velický, R.A.W. Dryfe, Functionalization of graphene at the organic/water interface, Chem. Sci. 6 (2015) 1316–1323.
[23] P.S. Toth, M. Velický, Q.M. Ramasse, D.M. Kepaptsoglou, R.A.W. Dryfe, Symmetric and asymmetric decoration of graphene: bimetal-graphene sandwiches, Adv. Funct. Mater. 25 (2015) 2899–2909.
[24] P.S. Toth, M. Velický, M.A. Bissett, T.J.A. Slater, N. Savjani, A.K. Rabiu, A.M. Rakowski, J.R. Brent, S.J. Haigh, P. O'Brien, R.A.W. Dryfe, Asymmetric MoS_2/graphene/metal sandwiches: preparation, characterization, and application, Adv. Mater. 28 (2016) 8256–8264.
[25] A.T. Valota, P.S. Toth, Y.-J. Kim, B.H. Hong, I.A. Kinloch, K.S. Novoselov, E.W. Hill, R.A.W. Dryfe, Electrochemical investigation of chemical vapour deposition monolayer and bilayer graphene on the microscale, Electrochim. Acta 110 (2013) 9–15.
[26] A.C. Ferrari, J.C. Meyer, V. Scardaci, C. Casiraghi, M. Lazzeri, F. Mauri, S. Piscanec, D. Jiang, K.S. Novoselov, S. Roth, A.K. Geim, Raman spectrum of graphene and graphene layers, Phys. Rev. Lett. 97 (2006).
[27] L.M. Malard, M.A. Pimenta, G. Dresselhaus, M.S. Dresselhaus, Raman spectroscopy in graphene, Phys. Rep. 473 (2009) 51–87.
[28] P.S. Toth, A.T. Valota, M. Velický, I.A. Kinloch, K.S. Novoselov, E.W. Hill, R.A.W. Dryfe, Electrochemistry in a drop: a study of the electrochemical behaviour of mechanically exfoliated graphene on photoresist coated silicon substrate, Chem. Sci. 5 (2014) 582–589.
[29] M. Velický, D.F. Bradley, A.J. Cooper, E.W. Hill, I.A. Kinloch, A. Mishchenko, K.S. Novoselov, H.V. Patten, P.S. Toth, A.T. Valota, S.D. Worrall, R.A.W. Dryfe, Electron transfer kinetics on mono- and multilayer graphene, ACS Nano 8 (2014) 10089–10100.
[30] A. Gutes, B. Hsia, A. Sussman, W. Mickelson, A. Zettl, C. Carraro, R. Maboudian, Graphene decoration with metal nanoparticles: towards easy integration for sensing applications, Nanoscale 4 (2012) 438–440.
[31] Z. Saghi, X. Xu, Y. Peng, B. Inkson, G. Möbus, Three-dimensional chemical analysis of tungsten probes by energy dispersive X-ray nanotomography, Appl. Phys. Lett. 91 (2007) 251906.
[32] P.A. Midgley, R.E. Dunin-Borkowski, Electron tomography and holography in materials science, Nat. Mater. 8 (2009) 271–280.
[33] S. Ghasemi, S.R. Hosseini, S. Nabipour, P. Asen, Palladium nanoparticles supported on graphene as an efficient electrocatalyst for hydrogen evolution reaction, Int. J. Hydrogen Energy 40 (2015) 16184–16191.
[34] A. Shen, Y. Zou, Q. Wang, R.A.W. Dryfe, X. Huang, S. Dou, L. Dai, S. Wang, Oxygen reduction reaction in a droplet on graphite: direct evidence that the edge is more active than the basal plane, Angew. Chem. Int. Ed. 53 (2014) 10804–10808.
[35] F.W. Campbell, S.R. Belding, R. Baron, L. Xiao, R.G. Compton, The hydrogen evolution reaction at a silver nanoparticle array and a silver macroelectrode compared: changed electrode kinetics between the macro- and nanoscales, J. Phys. Chem. C 113 (2009) 14852–14857.
[36] A.J. Bard, L.R. Faulkner, Electrochemical Methods, Fundamentals and Applications, 2nd ed., John Wiley & Sons, New York, 2001.
[37] S. Hu, M. Lozada-Hidalgo, F.C. Wang, A. Mishchenko, F. Schedin, R.R. Nair, E.W. Hill, D.W. Boukhvalov, M.I. Katsnelson, R.A. Dryfe, I.V. Grigorieva, H.A. Wu, A.K. Geim, Proton transport through one-atom-thick crystals, Nature 516 (2014) 227–230.
[38] B.E. Conway, B.V. Tilak, Interfacial processes involving electrocatalytic evolution and oxidation of H_2, and the role of chemisorbed H, Electrochim. Acta 47 (2002) 3571–3594.
[39] M.A. Bissett, I.A. Kinloch, R.A.W. Dryfe, Characterization of MoS_2–graphene composites for high-performance coin cell supercapacitors, ACS Appl. Mater. Interfaces 7 (2015) 17388–17398.
[40] K.-J. Huang, L. Wang, Y.-J. Liu, Y.-M. Liu, H.-B. Wang, T. Gan, L.-L. Wang, Layered MoS_2–graphene composites for supercapacitor applications with enhanced capacitive performance, Int. J. Hydrogen Energy 38 (2013) 14027–14034.
[41] Q. Cheng, J. Tang, J. Ma, H. Zhang, N. Shinya, L.-C. Qin, Graphene and nanostructured MnO_2 composite electrodes for supercapacitors, Carbon 49 (2011) 2917–2925.
[42] X. Cao, Y. Shi, W. Shi, G. Lu, X. Huang, Q. Yan, Q. Zhang, H. Zhang, Preparation of novel 3D graphene networks for supercapacitor applications, Small 7 (2011) 3163–3168.
[43] A. Winchester, S. Ghosh, S. Feng, A.L. Elias, T. Mallouk, M. Terrones, S. Talapatra, Electrochemical characterization of liquid phase exfoliated two-dimensional layers of molybdenum disulfide, ACS Appl. Mater. Interfaces 6 (2014) 2125–2130.
[44] J.J. Nieminen, I. Hatay, P. Ge, M.A. Mendez, L. Murtomaki, H.H. Girault, Hydrogen evolution catalyzed by electrodeposited nanoparticles at the liquid/liquid interface, Chem. Commun. 47 (2011) 5548–5550.
[45] S. Rastgar, H. Deng, F. Cortes-Salazar, M.D. Scanlon, M. Pribil, V. Amstutz, A.A. Karyakin, S. Shahrokhian, H.H. Girault, Oxygen reduction at soft interfaces catalyzed by in situ-generated reduced graphene oxide, ChemElectroChem 1 (2014) 59–63.
[46] L. David, R. Bhandavat, G. Singh, MoS_2/graphene composite paper for sodium-ion battery electrodes, ACS Nano 8 (2014) 1759–1770.